JBIC Journal of Biological Inorganic Chemistry (2024) 29:427–439
https://doi.org/10.1007/s00775-024-02053-1

ORIGINAL PAPER

Catalytic role of histidine-114 in the hydrolytic dehalogenation of chlorothalonil by *Pseudomonas* sp. CTN-3

Grayson Gerlich[1,2] · Callie Miller[2] · Xinhang Yang[3] · Karla Diviesti[1,2] · Brian Bennett[4] · Judith Klein-Seetharaman[5] · Richard C. Holz[2]

Received: 20 October 2023 / Accepted: 19 February 2024 / Published online: 26 May 2024

Abstract

Chlorothalonil (2,4,5,6-tetrachloroisophthalonitrile; TPN) is an environmentally persistent fungicide that sees heavy use in the USA and is highly toxic to aquatic species and birds, as well as a probable human carcinogen. The chlorothalonil dehalogenase from *Pseudomonas* sp. CTN-3 (Chd, UniProtKB C9EBR5) degrades TPN to its less toxic 4-OH-TPN analog making it an exciting candidate for the development of a bioremediation process for TPN; however, little is currently known about its catalytic mechanism. Therefore, an active site residue histidine-114 (His114) which forms a hydrogen bond with the Zn(II)-bound water/hydroxide and has been suggested to be the active site acid/base, was substituted by an Ala residue. Surprisingly, Chd^{H114A} exhibited catalytic activity with a k_{cat} value of 1.07 s^{-1}, ~ 5% of wild-type (WT) Chd, and a K_M of 32 μM. Thus, His114 is catalytically important but not essential. The electronic and structural aspects of the WT Chd and Chd^{H114A} active sites were examined using UV–Vis and EPR spectroscopy on the catalytically competent Co(II)-substituted enzyme as well as all-atomistic molecular dynamics (MD) simulations. Combination of these data suggest His114 can quickly and reversibly move nearly 2 Å between one conformation that facilitates catalysis and another that enables product egress and active site recharge. In light of experimental and computational data on Chd^{H114A}, Asn216 appears to play a role in substrate binding and preorganization of the transition-state while Asp116 likely facilitates the deprotonation of the Zn(II)-bound water in the absence of His114. Based on these data, an updated proposed catalytic mechanism for Chd is presented.

Grayson Gerlich and Callie Miller represents co-first authorship.

✉ Brian Bennett
brian.bennett@marquette.edu

✉ Judith Klein-Seetharaman
judith.klein-seetharaman@asu.edu

✉ Richard C. Holz
rholz@mines.edu

[1] Contribution from the Quantitative Biosciences and Engineering Program, Colorado School of Mines, Golden, CO 80401, USA

[2] Department of Chemistry, Colorado School of Mines, Golden, CO 80401, USA

[3] Department of Chemistry, Marquette University, Milwaukee, WI 53233, USA

[4] Department of Physics, Marquette University, 1420 W. Clybourn St, Milwaukee, WI 53233, USA

[5] School of Molecular Sciences, Arizona State University, Phoenix, AZ 85004, USA

Graphical abstract

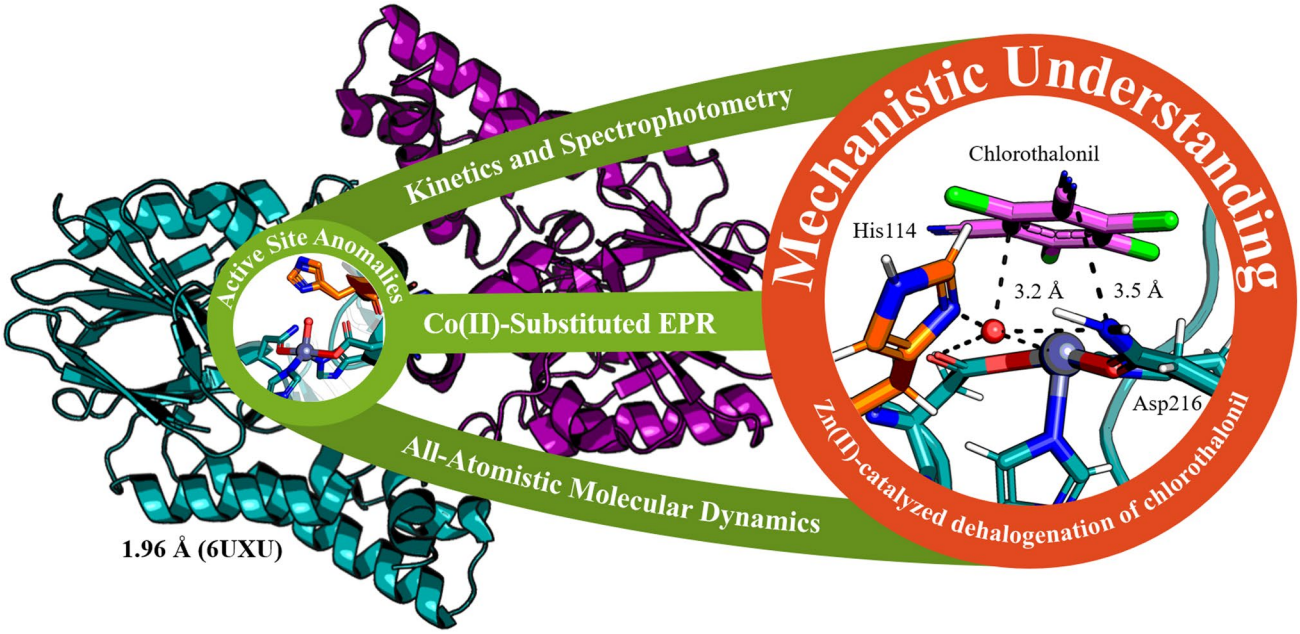

Keywords Dehalogenase · Electron paramagnetic resonance · Molecular dynamics · Zinc · Metalloenzyme · Chlorothalonil

Introduction

The enzymes that catalyze the hydrolytic dehalogenation of aromatic compounds have garnered attention over the past two decades for commercial and industrial applications, particularly for the bioremediation of persistent environmental contaminants [1–4]. The prevalence, toxicity, and recalcitrance to degradation of halogenated aromatics, combined with the unusual chemistry and undeniable utility of hydrolytic dehalogenases, make these enzymes an exciting target for study. Despite recent efforts to identify dehalogenase-containing bacteria and annotate their genomes, the cohort of experimentally studied hydrolytic dehalogenases—especially those that degrade aromatic halogenated species—remains relatively small [5–7].

Chlorothalonil dehalogenase (Chd, UniProtKB C9EBR5) is a Zn(II)-dependent, dimeric metalloenzyme that catalyzes the hydrolytic dehalogenation of chlorothalonil (TPN; 2,4,5,6-tetrachloro-isophthalonitrile), a broad-spectrum fungicide, to its corresponding less toxic aromatic alcohol (4-OH-TPN, 4-hydroxytrichloro-isophthalonitrile) (Scheme 1) [8]. Chd, originally discovered in *Pseudomonas* sp. CTN-3, has a unique sequence, with no more than 15% similarity to any other protein for which a structure has been determined [8]. Its substrate, TPN, is highly toxic to many aquatic species, damaging to soil environments and can cause birth defects in birds and mammals [9, 10]. It is strongly absorbed in soils, persistent on plant products, and can generate toxic and mobile metabolites [3, 11, 12]. It has also been classified as a possible human carcinogen by the EPA, which is especially concerning considering demonstrated TPN exposure to agricultural workers and detection in urban wastewater streams [13–16]. TPN was banned in the European Union in 2019, but between its environmental persistence and its continued, heavy use of > 5 million kg per year in the US, it remains a challenging environmental contaminant [16].

Chd is an important catalyst for the bioremediation of TPN; however, a lack of understanding surrounding its catalytic mechanism remains a major hurdle to its implementation in environmental remediation. The X-ray crystal structure of Chd (PDB: 6UXU) revealed an ~ 65 kDa homodimer with three zinc binding sites [8, 17]. One Zn(II)

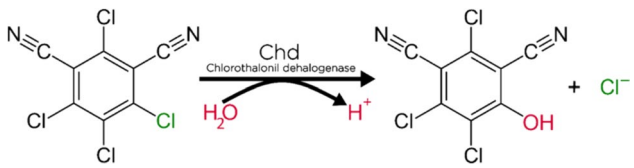

Scheme 1 Hydrolysis of TPN to 4-OH-TPN and chloride by Chd

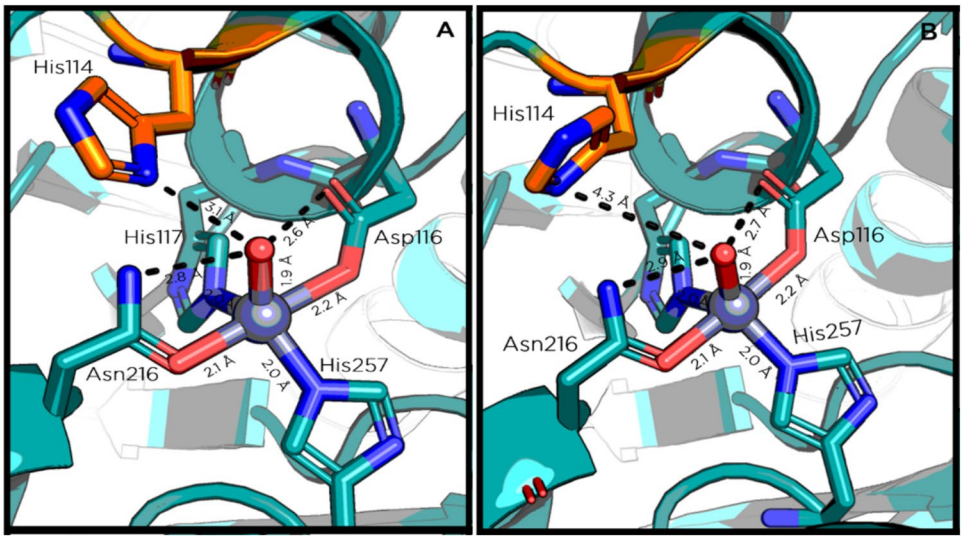

Fig. 1 **a** Chd active site in the His114a conformation. Zn(II) is represented as a grey sphere. **b** Chd active site in the His114b conformation. Key distances are shown in angstroms, calculations done in pdb2gmx

center is structural with a tetrahedral geometry coordinated by a histidine and an aspartic acid from each monomer, while the other two Zn(II) sites are the catalytic centers, one per monomer. Each active site Zn(II) ion resides in a distorted trigonal bipyramidal (TBP) geometry (Fig. 1) and lies within a B2 metallo-β-lactamase (MBL) type fold [8]. This Zn(II) ion is coordinated by His117, His257, Asp116, Asn216, and water/hydroxide as ligands (Fig. 1). His114 forms a hydrogen bond with the active site water/hydroxide moiety, similar to other MBLs like the carbapenemase from *Aeromonas hydrophila* (CphA) [18]. It was hypothesized that His114 acts as a general acid/base during the reaction cycle, accepting a proton from the Zn(II) bound water to generate a hydroxyl moiety for nucleophilic attack towards an ortho carbon of TPN [19]. Curiously, His114 occupies two distinct orientations in the X-ray structure, suggesting possible catalytically relevant motility (Fig. 1) [8]. The first conformation, His114(a), provides a hydrogen bond to the Zn(II)-bound water/hydroxide while the second conformation, His114(b), is rotated 90° effectively eliminating hydrogen bond formation with the Zn(II) bound water/hydroxide.

To investigate the catalytic role of His114, the His114Ala variant Chd enzyme (Chd^{H114A}), as well as the catalytically competent cobalt substituted variant, Co-Chd^{H114A}, were prepared and analyzed with a combined experimental and computational approach. Chd^{H114A}, surprisingly, retains ~ 5% of wild-type (WT) Chd activity, indicating His114 is catalytically important but not essential. UV–Visible spectroscopy (UV–Vis) and electron paramagnetic resonance (EPR) were performed with Co-Chd^{H114A}, while all-atomistic molecular dynamics (MD) simulations and docking studies were conducted with WT Chd and Chd^{H114A}. Together, these experiments were selected to gain insights into the electronic, structural, and dynamic properties of the Chd^{H114A} variant, as well as to contrast with similar work performed with WT Co-Chd [19]. These data provide critical insight into the catalytic mechanism of Chd, including other potential acid/base species within the active site.

Materials and methods

Materials. NEB restriction enzymes, XL10-Gold ultracompetent and BL21(DE3) competent cells, T4 DNA Ligase, and QuikChange II site-directed mutagenesis kits were purchased from Agilent Technologies. Five mL immobilized metal chelate affinity chromatography (IMAC) Ni–NTA columns were purchased from Qiagen. Wizard® SV gel, polymerase chain reaction (PCR) clean-up system and plasmid purification kits were purchased from Promega. Sodium dodecyl sulphate–polyacrylamide gel electrophoresis (SDS-PAGE) pre-cast gels and buffers were purchased from Bio-Rad Laboratories. Luria–Bertani (LB) broth, agar, isopropyl β-D-1-thiogalactopyranoside (IPTG), 4-(2-hydroxyethyl)-1-piperazineethanesulfonic acid (HEPES), tris (hydroxymethyl) aminomethane (Tris–HCl), potassium bromide, sodium chloride, cobalt chloride, zinc chloride, Bradford reagent, imidazole, potassium sodium tartrate, hydrochloric acid, sodium hydroxide, kanamycin, chloramphenicol, glycerol, 2,4,5,6-tetrachloroisophthalonitrile (chlorothalonil, TPN) and 4-hydroxy-2,5,6-trichloroisophthalonitrile (4-OH-chlorothalonil, 4-OH-TPN) were purchased as the highest purity available from either Thermo Fisher Scientific or Sigma Aldrich.

Mutagenesis. His114 was substituted by Ala (Chd^{H114A}) by a single mutagenic primer as follows: Sense primer: GTTAACACCAGCTATGCCGGTGATCACAG, antisense primer: CTGTGATCACCGGCATAGCTGGTGTTAAC. Mutated bases are underlined. The sense primer had a complementary sequence to the corresponding antisense primer.

The first PCR reaction was performed using the sense primer and antisense primer in separate tubes (25 µL). Following an initial denaturation at 98 °C for 1 min, 5 PCR cycles were carried out: each cycle was incubated at 98 °C for 15 s, followed by a 30 s annealing step at 63 °C, and a 1 min extension at 71 °C. A 50 µL mixture was prepared by combining both solutions for the second PCR reaction, which was carried out under the same conditions, but for 55 cycles. The final products were directly transformed into XL10-Gold ultracompetent *E. coli* cells. The mutated sequence was verified by DNA sequencing (Functional Biosciences Sequencing Team, Madison, WI).

Expression and purification of Chd. WT Chd was prepared and purified as previously reported [8]. For Chd^{H114A}, the pET28 + vector purified from XL10-Gold ultracompetent cells was transformed into BL21(DE3) competent *E. coli* cells. Approximately 40 g of cells were prepared and purified as described for WT Chd [8]. About 10 mg of soluble Chd^{H114A} enzyme was purified per 40 g of cells. SDS-PAGE gels revealed a single polypeptide band at ~ 33 kDa, in agreement with previous studies [8, 17]. Final Chd products were exchanged into 50 mM HEPES buffer at pH 7. The Chd concentration was determined using a Bradford assay and a standard curve was plotted using various concentrations of Chd reacted with Bradford assay reagent vs. the absorbance at 595 nm.

Spectrophotometric activity assay. The activity of WT Chd and Chd^{H114A} was measured at 25 °C using a Shimadzu UV-2600i spectrophotometer equipped with a Quantum Northwest t2 × 2 Sport temperature-controlled cell holder in 1 mL quartz cuvettes. A 1 mL reaction consisted of 50 mM HEPES buffer at pH 7.0 and various concentrations of TPN. The rate of TPN dehalogenation was determined by continuously monitoring the formation of 4-OH-TPN at 345 nm ($\Delta\varepsilon_{345} = 3500\ M^{-1}\ cm^{-1}$) [20]. The kinetic constants V_{max} and K_m were calculated by fitting the experimental data to the Michaelis–Menten equation by non-linear least-squares regression using Python (Python Software Foundation, Wilmington, DE). One unit of enzyme activity was defined as the amount of enzyme that catalyzed the production of 1 µmol of TPN per minute at 25 °C.

pH profiles. The enzymatic activity of ~ 25 µM Chd^{H114A} towards TPN was measured at pH values between 3 and 10. Different buffers were selected for their effective buffering range: borate (pH 8.5–10), Tris–HCl (pH 7.2– 8.5), HEPES (pH 6.8–7.2), MES (pH 5.5–6.5), and acetate (pH 3.0–5.5). The kinetic parameters k_{cat}, K_M, and k_{cat}/K_M were determined using seven different substrate concentrations ranging from 0 to 400 µM at each pH studied. Kinetic parameters and fits to the kinetic curves were obtained using non-linear least-squares regression with Python. When transitioning between buffers, experiments were run at identical pH values but in different buffers with no observed effect on kinetic parameters [17].

Electron paramagnetic resonance (EPR). Apo-enzyme was prepared using previously published zinc removal methods [19]. Apo-WT Chd and Apo-Chd^{H114A} were incubated with 2 eq $CoCl_2$ (per dimeric protein), which was shown in prior studies to fully metallate Apo-WT Chd, for 30 min prior to freezing in liquid nitrogen [19]. EPR spectra were recorded on a Bruker EMX-AA-TDU/L spectrometer equipped with an ER4112-SHQ resonator (~ 9.45 GHz) and an HP 5350B microwave counter for precise frequency measurement. Cryogenic temperatures were maintained using a Bruker/ColdEdge Stinger-5 K recirculating helium refrigerator and an Oxford Instruments Mercury iTC temperature controller. Rapid passage spectra were recorded in phase quadrature ($\phi = 90°$) with second-harmonic phase-sensitive detection ($\partial^2\chi''/\partial B^2$). EPR spin Hamiltonian parameters were obtained from computer simulation as described earlier [19, 21], using EasySpin and MATLAB [22, 23].

All-atomistic molecular dynamics simulations (MD). All simulations were performed in GROMACS 2022.3 [24, 25]. The CHARMM36 force field was used, and the system solvated explicitly with the sTIP3P water model [26]. The preparation and execution of production MD runs largely followed established methods [27]. Briefly, the Chd dimer crystal structure (PDB: 6UXU) was prepared using the pdb-2gmx tool in GROMACS and the active-site Zn ions were merged with their respective chains, while the structural-site Zn(II) ion was merged with only one of the monomers for simplicity. The dodecahedral solvent box contained 90,868 atoms, with 27,161 solvent molecules, at neutral charge and 100 mmol NaCl to loosely mimic an isotonic salt concentration. For all simulations, the time step was 2 fs, energies and coordinates were saved every 10 ps, and particle mesh Ewald long-range electrostatics were used. Energy minimization was performed until the maximum system force was < 10 kJ/(mol*nm), which is about the root mean square (RMS) force exhibited by a nitrogen and a proton modeled as a weak harmonic oscillator at room temperature. Following this, the system was subjected to pressure and temperature equilibration with a modified Berendsen thermostat and C-rescale pressure coupling. Zn(II) cations were treated with a non-bonding model, which has been used for other MBLs [28, 29]. The incorporation of PDB-derived bond and dihedral information, as included in CHARMM36, was shown to cause a significant disruption of the distorted TBP geometry around the Zn(II) ion, so these constraints were not explicitly modeled [30]. To investigate and verify the stability of Zn(II) in the active site, 100 ns simulations of apo-WT Chd and apo-Chd^{H114A} were performed following the same methodology as above.

Umbrella sampling to calculate the potential of mean force (PMF) was performed with the same step (2 fs)

and write (10 ps) intervals as above using the Accelerated Weight Histogram (AWH) functionality built into GROMACS. For His114-Zn(II), the pull coordinate was between the N^{δ} nitrogen of His114 and Zn(II), from 4.0 Å to 8.0 Å. AWH umbrella sampling was also done with Asn216 to investigate its dissociation behavior. For Asn216-Zn(II), the pull coordinate was between the carboxamide oxygen of Asn216 and Zn(II), from 1.8 Å to 4.5 Å (Figure S2). These data were processed in Python, and most simulations were performed on an in-house computer cluster. Additional CPU time was provided by NMRbox, a Biomedical Technology Research Resource (BTRR), which is supported by NIH grant P41GM111135 (NIGMS) [31].

Docking. All frames from a 100 ns GROMACS simulation of WT Chd were processed for docking studies. All solvating molecules were removed except for the active site water and a second water that was transiently coordinated by Zn(II). Receptor and ligand structures were prepared by SPORES (included within PLANTS) using the complete setting and the second active site water was treated as switchable because the position is filled transiently. There were no differences between poses generated with one water versus those generated with a switchable second water. Poses generated with a non-switchable second water had docking scores > 10 lower than those generated with one water, or a switchable second water. Docking was performed using PLANTS with the CHEMPLP scoring function and speed1, where the binding site was defined as a sphere with a radius of 10 Å centered on the active site water, which sits close to the center of the active site pocket identified in the structure and simulations. Additional tuning was done using M3 parameters as published [32]. Docking results were sorted by three metrics: the distance in Å between the nitrile nitrogen of TPN and the sidechain nitrogen of Asn216, the distance in Å between the ortho carbon of TPN and the active site water, and the docking score provided by PLANTS. Poses were selected based on the minimization of the first two metrics, and the maximization of the third.

Results and discussion

The two different conformations of His114 observed in the X-ray crystal structure (Fig. 1), suggest trapped dynamic states or differences in His114 protonation states, either of which are likely mechanistically important. To investigate the catalytic role of His114, it was substituted by an Ala residue, eliminating its ability to form a hydrogen bond with the Zn(II)-bound water/hydroxide moiety. Inductively coupled plasma atomic emission spectroscopy (ICP-AES) analysis of the Chd^{H114A} variant revealed ~ 1.52 equivalents of zinc per monomer, representing fully metalated enzyme. Kinetic analysis of the Chd^{H114A} variant in 50 mM HEPES buffer, pH 7.0 indicated that it retained catalytic activity with a k_{cat} value of 1.51 ± 0.07 s^{-1} and a K_M value of 102 ± 39 µM ($k_{cat}/K_M = 1.5 \times 10^4$ M^{-1} s^{-1}) compared to WT Chd, which has a k_{cat} value of 24 ± 2 s^{-1} and a K_M value of 110 ± 30 µM ($k_{cat}/K_M = 2.2 \times 10^5$ M^{-1} s^{-1}) [19]. While the observed k_{cat} value is ~ 94% lower than that observed for WT Chd [17], the measurable and reproducible activity retained by Chd^{H114A} suggests that His114, while catalytically important, is not essential for catalytic activity and thus cannot be the sole general acid/base.

Ionization constants were previously determined for WT Chd by monitoring the pH dependence of the kinetic parameters k_{cat}, K_M, and k_{cat}/K_M over the pH range 4–10 [17]. Bell-shaped curves were observed with maximum catalytic activity in the pH range 6.5–9.2. Ionization constants for the ES complex were reported to be $pK_{ES1} = 5.4 \pm 0.2$ and $pK_{ES2} = 9.9 \pm 0.1$ while the ionization constants for the free enzyme or free substrate were $pK_{E1} = 5.4 \pm 0.3$, and $pK_{E1} = 9.5 \pm 0.1$. These ionization constants were assigned to a His residue for the acidic limb and possibly the Zn(II)-bound water for the basic side of the pH curve or the Asn216 ligand, which forms a hydrogen bond to the axial Zn(II)-bound water molecule, and whose pK_a for the NH_2 moiety in the free amino acid is ~ 9. The pH dependence of the kinetic parameters k_{cat}, K_M, and k_{cat}/K_M for the Chd^{H114A} variant was determined over the pH range 3–10. Bell-shaped curves were observed by the graphs of $\log\left(k_{cat}\right)$ and $log\left(\frac{k'_{cat}}{K'_M}\right)$ vs. pH (Fig. 2) and were fit to Eqs. 1 and 2, respectively [33]. Where k'_{cat} and $\left(\frac{k'_{cat}}{K'_M}\right)$ represent the maximum observed catalytic constant and catalytic efficiency, respectively. Ionization constants for the Chd^{H114A} variant were found to be $pK_{ES1} = 2.9 \pm 0.1$ and $pK_{ES2} = 10.3 \pm 0.2$ for the ES complex while ionization constants of $pK_{E1} = 3.8 \pm 0.1$, and $pK_{E1} = 9.4 \pm 0.1$ were obtained for the free enzyme or free substrate. Interestingly, the observed ionization constants for the acidic limb of the ES complex of the Chd^{H114A} variant are significantly lower than those of WT Chd (3 vs 5.4) consistent with the assignment of the WT Chd pK_{ES1} to a His residue, specifically His114. A new pK_{ES1} was observed for the Chd^{H114A} variant at ~ 3.0 with a pK_{E1} of 3.8 that was obscured in the WT Chd enzyme. This pK_a likely corresponds to an active site Asp

$$\log\left(k_{cat}\right) = \log\left(\frac{k'_{cat}}{1 + 10^{pK_{ES1} - pH} + 10^{pH - pK_{ES2}}}\right) \quad (1)$$

$$\log\left(k_{cat}/K_M\right) = \log\left(\frac{\left(\frac{k'_{cat}}{K'_M}\right)}{1 + 10^{pK_{E1} - pH} + 10^{pH - pK_{E2}}}\right) \quad (2)$$

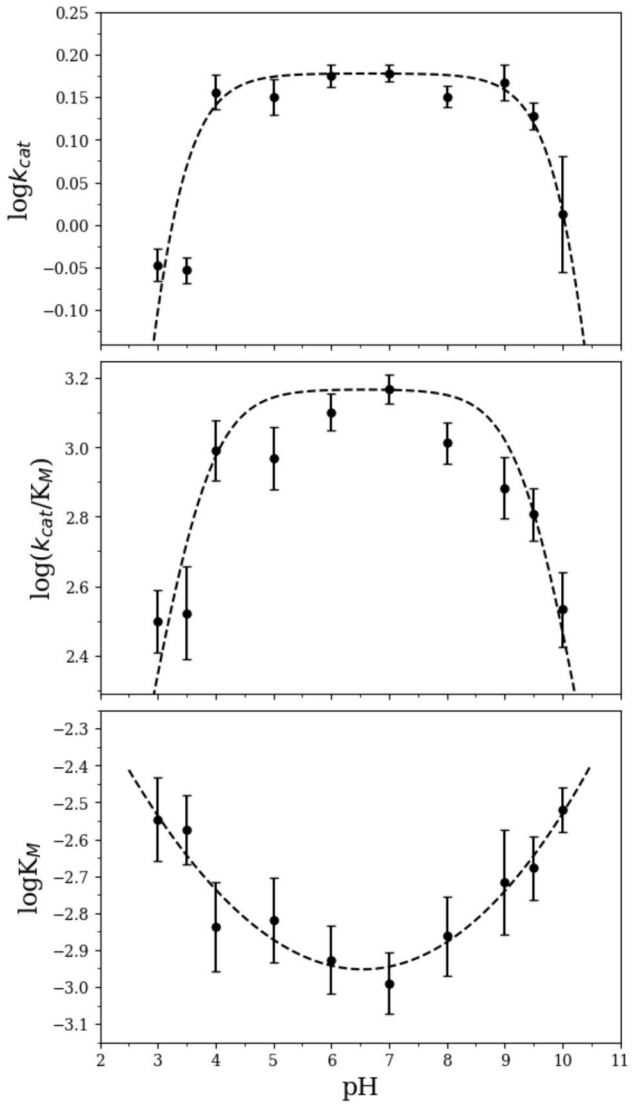

Fig. 2 pH dependent kinetics assay of Chd^{H114A}. Each data point was obtained in triplicate. Error bars represent the standard deviation of the Michaelis–Menten parameters fit from plots of reaction velocity vs TPN concentration, adjusted for the log scale according to ISO/IEC Guide 98–3:2008 [46]. The plot of k_{cat} versus pH was fit to Eq. 1, and the plot of k_{cat}/K_M versus pH was fit to Eq. 2. The plot of K_M versus pH was fit with a polynomial equation

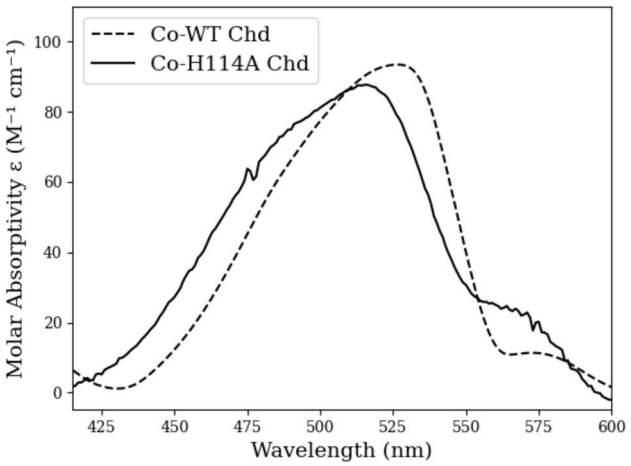

Fig. 3 UV–Vis absorption spectra of Co-WT Chd (dotted trace) and Co- Chd^{H114A} (solid trace)

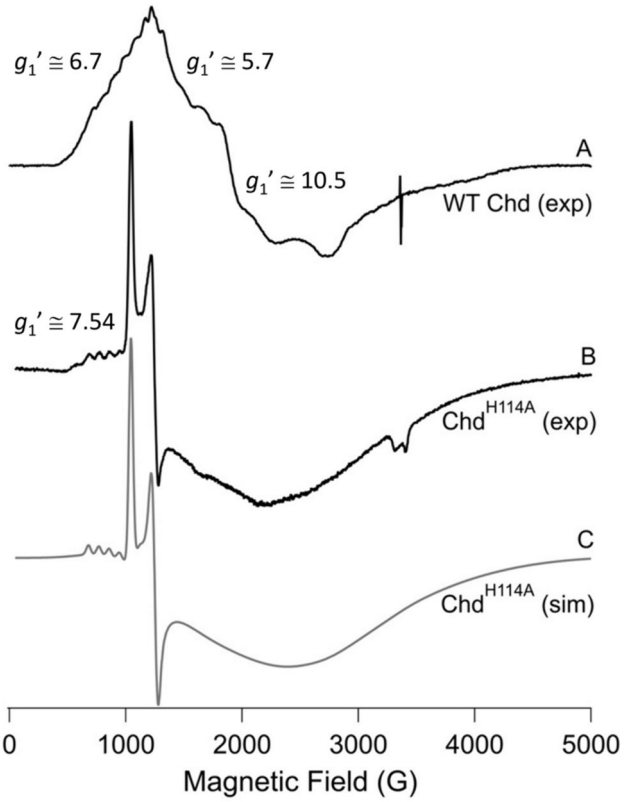

Fig. 4 EPR of Co(II)-substituted WT Chd and Chd^{H114A}. **a** EPR spectrum of WT Chd recorded at 12 K, 2 mW microwave power, and 12 G magnetic field modulation. **b** EPR spectrum of Chd^{H114A} recorded at 5.5 K, 5 mW microwave power, and 12 G magnetic field modulation

or Glu residue, which exhibit pK_as between 3.9 and 4.1 for the free amino acid. The most likely candidate for this pK_a is Asp116, which is a Zn(II) ligand and forms a hydrogen bond to the axial Zn(II)-bound water molecule. The basic limb values observed for the Chd^{H114A} variant are nearly identical to those observed for WT Chd, suggesting the same moiety, Asn216 or the Zn(II)-bound water molecule, is responsible for this pK_a.

To gain insight into the residual activity of the Chd^{H114A} variant, the structural and electronic properties of the active site of Chd^{H114A} were studied by EPR and UV–Vis spectroscopy, using the catalytically competent Co(II)-substituted forms of WT Chd and the Chd^{H114A} variant. The Co(II)-substituted WT Chd enzyme containing

one eq. of Co(II) per monomer (Co-Chd), exhibited a broad absorption band with a maximum at 535 nm ($\varepsilon_{535} = \sim 95\ M^{-1}\ cm^{-1}$) along with shoulders at 500 nm ($\varepsilon_{500} = \sim 70\ M^{-1}\ cm^{-1}$) and 580 nm ($\varepsilon_{580} = \sim 10\ M^{-1}\ cm^{-1}$) (Fig. 2) [19]. These data suggest that the Co(II) ions in Co-Chd reside in a pentacoordinate environment [21, 34], consistent with X-ray crystallographic data for WT Chd, which indicates a pentacoordinate, mononuclear Zn(II) active site [8]. The UV–Vis spectrum of the Co(II)-substituted Chd^{H114A} variant containing one eq. of Co(II) per monomer (Co-Chd^{H114A}) also exhibited broad absorption bands, one with a maximum at 520 nm ($\varepsilon_{595} = \sim 85\ M^{-1}\ cm^{-1}$) along with shoulders at 485 nm ($\varepsilon_{545} = \sim 70\ M^{-1}\ cm^{-1}$) and 560 nm ($\varepsilon_{515} = \sim 20\ M^{-1}\ cm^{-1}$) (Fig. 3). These data show a distinct blue shift from the WT Co-Chd UV–Vis spectrum but are still consistent with Co(II) in a pentacoordinate environment. The blue shift likely reflects the loss of the hydrogen bonds between His114 and the Zn(II)-bound water molecule, which would result in a slight decrease in the Lewis acidity of the Zn(II) ion.

The EPR spectrum of Co(II)-substituted WT Chd (Fig. 4a), as previously described in detail [19], is complex. The signal exhibited no marked temperature dependence over 5–20 K and was optimally detected at 12 K and 2 mW microwave power. The spectrum contains at least three distinct $S = {}^3/_2$ Co(II) signals that overlap extensively, precluding precise parameterization: an $M_S = \pm {}^1/_2$ signal exhibited a resolved ~ 94 G ^{59}Co hyperfine pattern centered at $g_1' \cong 6.7$ (most clearly discernible in the $\partial^2\chi''/\partial B^2$ spectrum [19]); an additional broad $M_S = \pm {}^1/_2$ signal with $g_1' \cong 5.7$ and devoid of a ^{59}Co hyperfine pattern; and an $M_S = \pm {}^3/_2$ signal with $g_1' \cong 10.5$ ($g_z = 2.75$) and $A_1(^{59}\text{Co}) \cong 110$ G, that may be associated with a high-field broad resonance at $g_3' \cong 1.8$. On the other hand, the EPR spectrum of Co-Chd^{H114A} (Fig. 4b) was clearly distinct from that of WT Co-Chd. The spectrum exhibited two well resolved signals; one with two sharp resonances at 1040 G and 1250 G, and the other exhibiting the first four resonances due to a ^{59}Co hyperfine splitting (hfs) pattern centered at 895 G ($g = 7.54$) (Fig. 4b) with $A(^{59}\text{Co}) \approx 92$ G. The hyperfine-split signal was modeled as an $M_S = \pm {}^3/_2$ species ($D < 0$), on the basis of the lack of associated $g\perp$ resonances in the spectrum and the fast relaxation (vide infra), with $g_z = 2.27$ and an A_z ^{59}Co hyperfine interaction of 280 MHz (Figure S1, Species S2; Table S1). As resonances from only one orientation, z, were observed, these g_z and A_z parameters are estimates and the other parameters ($g_{x,y}$, $A_{x,y}$, and E/D) are undetermined. This signal was clearly observed at 5.5 K (and 5 mW; Fig. 4b) but was not observable at 12 K due to fast relaxation. The other well-resolved signal exhibited no marked temperature dependence from 5 to 15 K and was modeled, assuming axial $\boldsymbol{g}$-symmetry, using $M_S = \pm {}^1/_2$ ($D > 0$), $g\perp = 2.97$, $g\perp = 2.27$, and $E/D = 0.06$ (Figure S1, Species S1; Table S1). The narrow line widths of each of these otherwise very distinct signals suggests that Co(II)

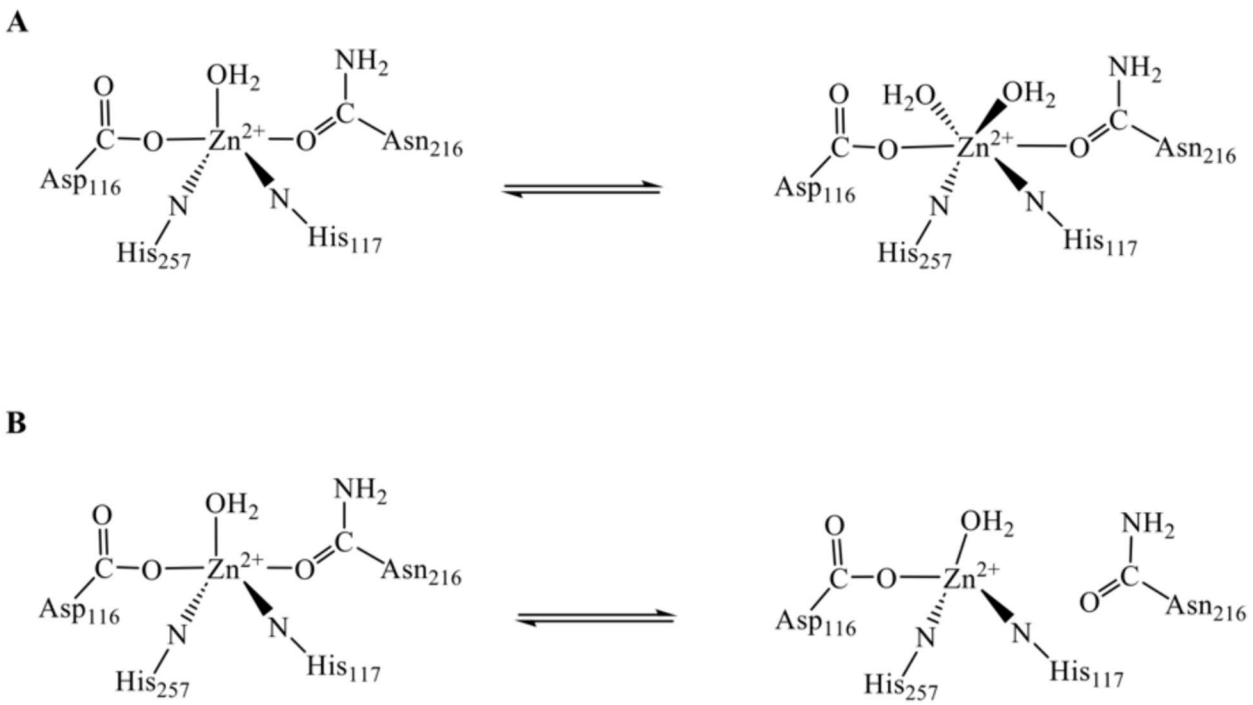

Fig. 5 Schematic of the coordination number changes observed in MD simulations. **a** Shows that addition of a water molecule forming a six-coordinate active site while **b** Shows the loss of the asparagine ligand forming a four-coordinate active site

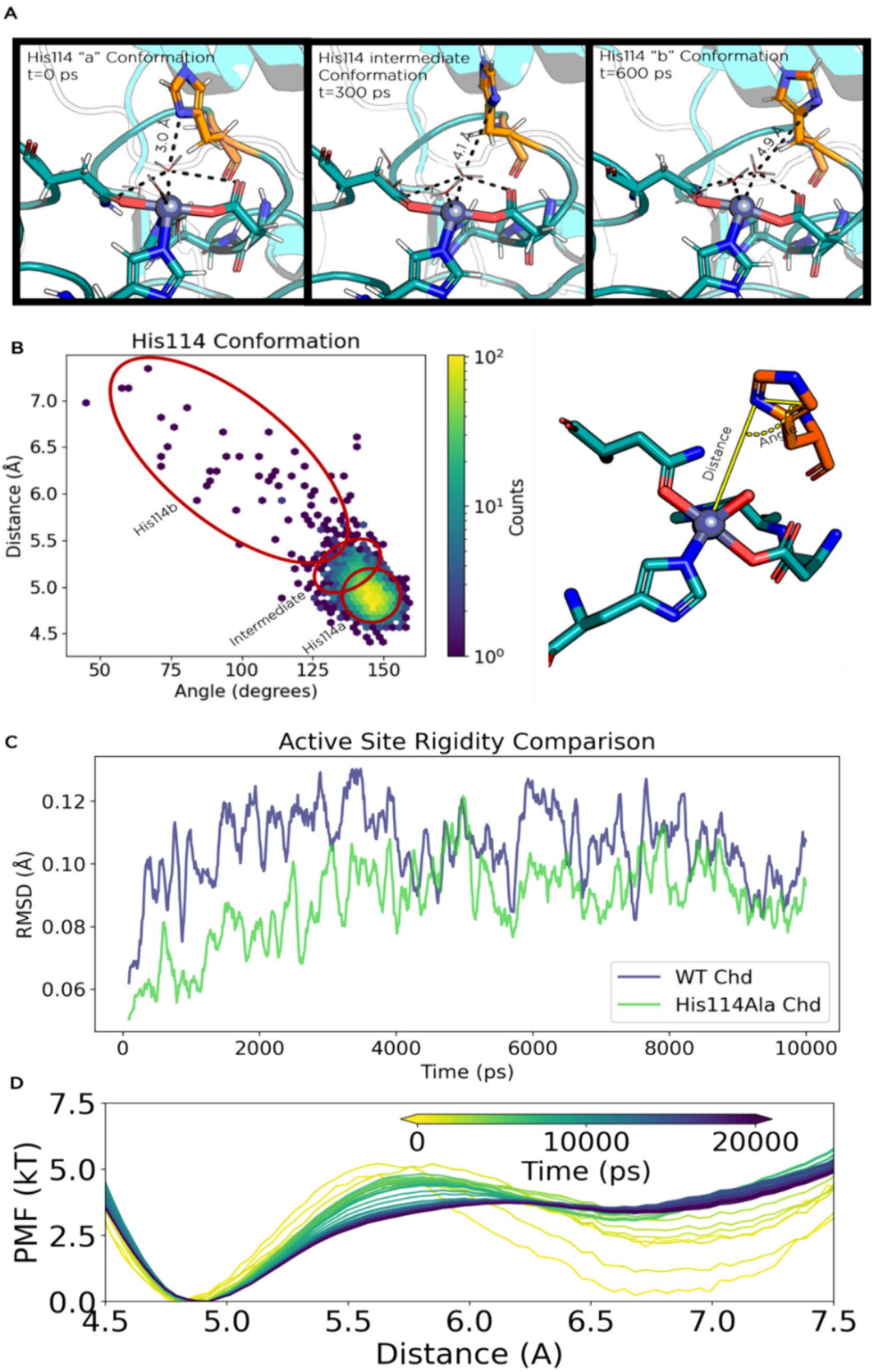
A
His114 "a" Conformation
t=0 ps
3.0 Å
His114 intermediate
Conformation
t=300 ps
4.1 Å
His114 "b" Conformation
t=600 ps
4.9 Å
B
His114 Conformation
Distance (Å)
Angle (degrees)
His114b
Intermediate
His114a
Counts
Distance
Angle
C
Active Site Rigidity Comparison
RMSD (Å)
Time (ps)
WT Chd
His114Ala Chd
D
PMF (kT)
Distance (A)
0
10000
20000
Time (ps)

◂**Fig. 6** **a** Chd active site in three poses selected to represent His114 conformations. His114 is visualized as orange sticks. Black dashed lines represent hydrogen bonds. Only those waters which form hydrogen bonds with active site residues are visualized. **b** Heatmap showing the conformational space sampled by His114. **c** RMSD deviations of Zn(II) coordinating residues in WT Chd and Chd^{H114A} vs their crystal structure positions over time. **d** Potential of Mean Force curves taken at different times from an AWH umbrella sampling experiment. The distance is measured from the Nδ of His114 to Zn(II) in Å

bound in the active site of Chd^{H114A} can adopt two distinct coordination environments, each of which is highly constrained, in marked contrast to WT Chd as well as the resting state of many Co-substituted Zn-metallohydrolases [21].

The rigidity of the active site and the origins of the two EPR species with resolved ^{59}Co hfs in WT Co-Chd were hypothesized to be due to different conformations of His114 or a bound water vs. hydroxyl ligand [19]. The two distinct resolved EPR signals from Co-Chd^{H114A} cannot, obviously, arise from distinct conformations of His114 as it is absent. Since the active site Zn(II) ion is five-coordinate with a distorted TBP geometry, it is possible that the two observed EPR signals are due to berry pseudorotations, where rapid exchange between TBP and square based pyramidal (SBP) geometry is occurring. In a small molecule model, this pseudo rotation requires about 3.6 kcal/mol [35]; for comparison, the energy required for the rotational conformation change of His114 is on the order of 2.4 kcal/mol. Thus, a Berry rotation would also be an energetically feasible option to explain the two EPR species. This explanation is not supported, however, though also perhaps not refuted, by the very narrow lines of the two EPR signals that would be expected to be broadened significantly by any coordination flexibility due to freezing out of multiple vibrational (pseudorotational) substates (*i.e.*, strains in $\boldsymbol{g}$, **D**, and **A**). An alternative explanation is that the Co(II) ion can adopt either 4- or sixfold coordination, resulting in $D<0$ and $D>0$, respectively and, perhaps, related to the lack of ^{59}Co hfs in the $D>0$ species. Six-coordinate Co(II) has been observed for species that exhibit penta-coordination in the analogous Zn(II) species [21]. In proteins, however, this appears to occur due to coordination of a water molecule which, again, would be expected to result in broad EPR resonances.

In addition to the well-resolved signals in the Co(II) EPR spectrum of Chd^{H114A}, there was also a broad EPR absorption across the 0–6000 G spectral envelope. This absorption exhibited some temperature-dependent intensity variation that suggested relaxation effects. To probe this, second-harmonic phase quadrature EPR spectra were collected. In the absence of rapid-passage effects (slow relaxation on the EPR timescale), no signal would be expected with the phase-sensitive detection out of phase with the field modulation. Under rapid passage conditions, a signal *is* observed that can contain mixtures of the derivative and absorption signal, which is very sensitive to precise experimental conditions. Two examples of such signals from Chd^{H114A} are presented in Figure S1 (bottom two traces) and provided the basis for two modeled spectra (Figure S1, Species S3 and S4; Table S1) that were included in the overall simulation (Fig. 4c) of the Chd^{H114A} spectrum. The origins of this very broad, slow-relaxing EPR absorption are as yet unclear, although analogous EPR absorption was observed in WT Chd coordinated by the inhibitor tetrachloroterephthalonitrile [19].

The two conformations of His114 and its role in the catalytic mechanism of TPN hydrolysis by Chd were further investigated with all-atomistic molecular dynamics (MD) simulations (Fig. 5). The WT Chd dimer was stable at microsecond timescales (1 μs) and barely deviated from the crystal structure over time (backbone RMSD ≈ 1 Å). In the active site, the residues coordinating the Zn(II) ion (Asp116, His117, Asn216, and His257) also deviated little from their crystal positions (< 1 Å) over the course of this simulation. Interestingly, the active site Zn(II) coordination geometry was able to distort allowing Zn(II) to access an octahedral, six-coordinate, geometry (Fig. 6a) [29]. In this conformation, the axial ligands (Asp116 and Asn216) remain in position, while the angle between the equatorial histidine ligands decreases from ~ 125° to ~ 90° allowing a water molecule to occupy a sixth coordination position. These data suggest a mixture of five and six-coordinate active site Co(II) ions, which would be consistent with the observed EPR spectrum of Co-Chd^{H114A}. In this position, the water is inaccessible to TPN due to the geometry of the active site, so its catalytic relevance is likely limited, consistent with previous EPR studies of inhibitor-bound Co(II)-substituted Chd, which indicated that TPN binding does not change the coordination number of Zn(II) [19].

Based on MD simulations, His114 preferentially adopts the His114a conformation, where the N^{δ} of His114 forms a hydrogen bond (3.0 Å) with the Zn(II)-bound water/hydroxide (Fig. 6a). It accesses the His114b conformation transiently, passing through an intermediate state where the imidazole ring remains in plane with the Zn(II) center (Fig. 6a, Video S1). In this intermediate state, the hydrogen bond between the N^{δ} of His114 and the active site water has a length > 3 Å. Hydrogen bonds greater than 3 Å are generally considered weak, with a $\Delta G_{formation} > -1$ kcal/mol, as compared to average strength of the hydrogen bonds that contribute to protein structure (-2 ± 1 kcal/mol) [36]. Because the imidazole ring of His114 does not rotate until after this distance threshold is reached, the weakening and breaking of this hydrogen bond is required for adoption of the His114b conformation (Fig. 6b, Video S1). The change in potential of mean force (PMF) between the N^{δ} of His114 and Zn(II) indicates that His114a represents a stable energy

minimum, normalized to 0 kT, while His114b represents a metastable plateau in the PMF with a transition barrier of about 4 kT (about 2.4 kcal/mol at 298 K) (Fig. 6d). This barrier is consistent with the strength of one hydrogen bond, indicating that breaking the hydrogen bond between the N^{δ} of His114 and the active site water is the key energetic barrier for this conformational change [36]. The stability of the His114b conformation, then, must result from further stabilizing interactions between His114b and solvent or other residues in the active site pocket. In the His114b conformation (Fig. 6a), N^{δ} can form three hydrogen bonding interactions to solvating waters. Moreover, recent quantum chemical analyses of high-resolution neutron structures have revealed that histidine residues can form strong and stable C-H-O interactions without compromising the capability of imidazole nitrogen atoms to form hydrogen bonds [37]. These interactions likely further stabilize the His114b conformation. Should the active site water/hydroxide be removed—either by diffusion or catalysis—His114 would be free to rotate into the His114b conformation, as there would be no hydrogen bond supporting the His114a conformation. These data suggest that these two conformations, His114a and His114b, are related to the protonation state of the Zn(II) bound water. In carbonic anhydrase, the pK_a of bound water molecule (which becomes the nucleophilic hydroxyl) is 7.5 [38]. This is much lower than the pK_a of an aqueous water molecule ($pK_a \cong 14$), indicating a more facile release of the proton in the Zn(II) bound water [39]. The rotation of His114 does free the metal center for recharge after catalysis, and possibly assists 4-OH-TPN in exiting the active site [8].

The Chd^{H114A} variant was created computationally and the coordination geometry of the Zn(II) in simulation appears identical to that of WT Chd. The residues coordinating the Zn(II) center exhibit less motion and higher rigidity in the Chd^{H114A} variant as compared to WT Chd, as shown by comparing the all-heavy-atom RMSD over time for the respective residues, wherein the RMSD of Chd^{H114A} is, on average, 0.2 Å less than WT Chd (Fig. 6c). This is perhaps counterintuitive, as the removal of a coordinating interaction from the active site actually increases rigidity. These data, however, agree with EPR data in that they are consistent with a more rigid active site in Chd^{H114A}. Because Zn(II) is treated as a non-bonding model in simulation, the ligand binding strength is not represented. Therefore, the MD and EPR data together suggest that the *presence* of His114 in the active site and the resultant hydrogen bonding network strains the active site geometry to allow additional mobility, *i.e.,* increased microheterogeneities. In the absence of evidence suggesting that a change in coordination state occurs during catalysis and considering that TPN does not directly bind to the Zn(II) center, an alternate general acid/base in the active site must be considered.

Of the other active site residues within hydrogen bonding distance of the active site water, Asp116 and Asn216 are possible candidates that could assist [19]. Asparagine is an unlikely metal-binding ligand from an evolutionary perspective and, hence, an unlikely general acid/base, as it is extremely rare as a ligand in bioinorganic systems [40–42]. Ligand-field theory predicts that asparagine is a weaker-field ligand compared to histidine due to possible π-donation into Zn(II) π*-orbitals from the carboxamide oxygen, which has been confirmed experimentally [43]. As a result, Asn216 likely has a lower affinity for Zn(II) and the Asn216-Zn(II) bond is predicted to be the weakest of the coordinating interactions in the Chd active site. This was confirmed during MD simulations as the Asn216 ligand was prone to dissociation, generating a more open, four-coordinate active site conformation. Thus, the Asn216-Zn(II) bond was restrained using a simple harmonic restraint with mean distance 2.1 Å (as per the crystal structure). The upper bounds (up1 and up2) of the restraint were 2.3 and 2.5 Å respectively. This restraint prevented Asn216 from accessing a stable non-bonded configuration away from the metal center (Figure S2). The relative stabilities of the conformations with and without forced Asn216-Zn(II) binding vary throughout the simulation, but the average barrier to transition between the bound and unbound conformations is about 10 kT (about 5.9 kcal/mol) (Figure S2). This is a higher energy barrier than the average hydrogen bond in a protein structure, but much less than most covalent interactions [29]. A four-coordinate geometry could also be consistent with the observed EPR data for the Co-substituted Chd^{H114A} variant.

Two conserved asparagines (*e.g.*, Asn116 and Asn233 in CphA) that are present in similar MBL systems participate in the active site hydrogen bonding network and interact with product intermediates, but are not strictly critical for catalysis [18, 42, 44]. Neither, however, are direct analogs of Asn216 in Chd, because they do not coordinate the metal center. It is, therefore, a distinct possibility that the role that Asn216 in Chd evolved to facilitate TPN coordination and has previously been proposed as a possible TPN-binding partner [19]. As such, Asn216 likely plays a role in positioning TPN through a hydrogen bond between a TPN -CN group and the $-NH_2$ moiety of Asn216. Such an interaction would prearrange the transition-state for catalysis and also activate the CN bond, decreasing the CN triple-bond character, resulting in a partial positive charge on the carbon atom of the C–Cl bond that will be hydrolyzed. To test the feasibility of this substrate binding model, docking studies were performed on conformational snapshots taken from MD simulations of WT Chd. Docking studies were performed using PLANTS, which has been identified as a more effective docking algorithm for Zn metalloproteins than AutoDock Vina, which has also been used to study Chd [8, 32, 45]. Figure 7 shows the optimal docking pose generated

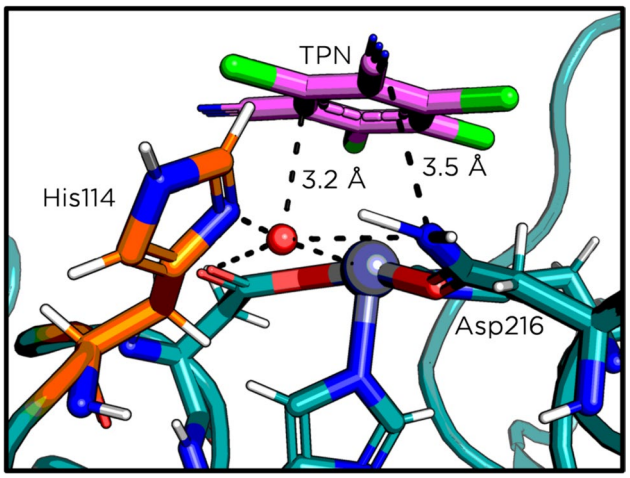

Fig. 7 Snapshot of the Chd active site taken from AA-MD simulation of WT Chd with docked TPN visualized as violet sticks, His114 as orange sticks, and other active site residues as teal sticks. The proposed interactions between Asn216 and the nitrile nitrogen of TPN (3.5 Å) and the active site water and an ortho carbon of TPN (3.2 Å) are visualized as black dotted lines, as are the Zn-water, Asp116-water, Asn216-water, and His114-water interactions

using PLANTS. While docking programs are known to have difficulty accurately predicting how substrates will bind to transition metals, in this case, the position of TPN in the Chd active site is mostly governed by steric interactions from His114 and Trp227. Additionally, the entire enzyme is modelled and included in dynamics to allow relaxation into a dynamic equilibrium from the crystal position. In this docking pose, the nitrile nitrogen of TPN associates with Asn216 (3.5 Å) while the active site water moiety is in a position for nucleophilic attack on the ortho carbon of TPN (3.2 Å). The proposed hydrogen bond between TPN and Asn216 orients TPN in the active site, preserves the active site water as a nucleophile, and helps to remove electron density from the aromatic ring of TPN to make the ortho carbon more susceptible to nucleophilic attack. This also agrees with published EPR data that suggest that the metal center does not change coordination state upon substrate binding [19]. Therefore, in the absence of His114, Asp116 is proposed to play the role of general acid/base during catalytic turnover, as it forms a hydrogen bond with the Zn-bound water/hydroxide (2.6 Å). This is supported by the basic pK_a observed for Chd^{H114A}, the significantly stronger hydrogen bonding interaction for

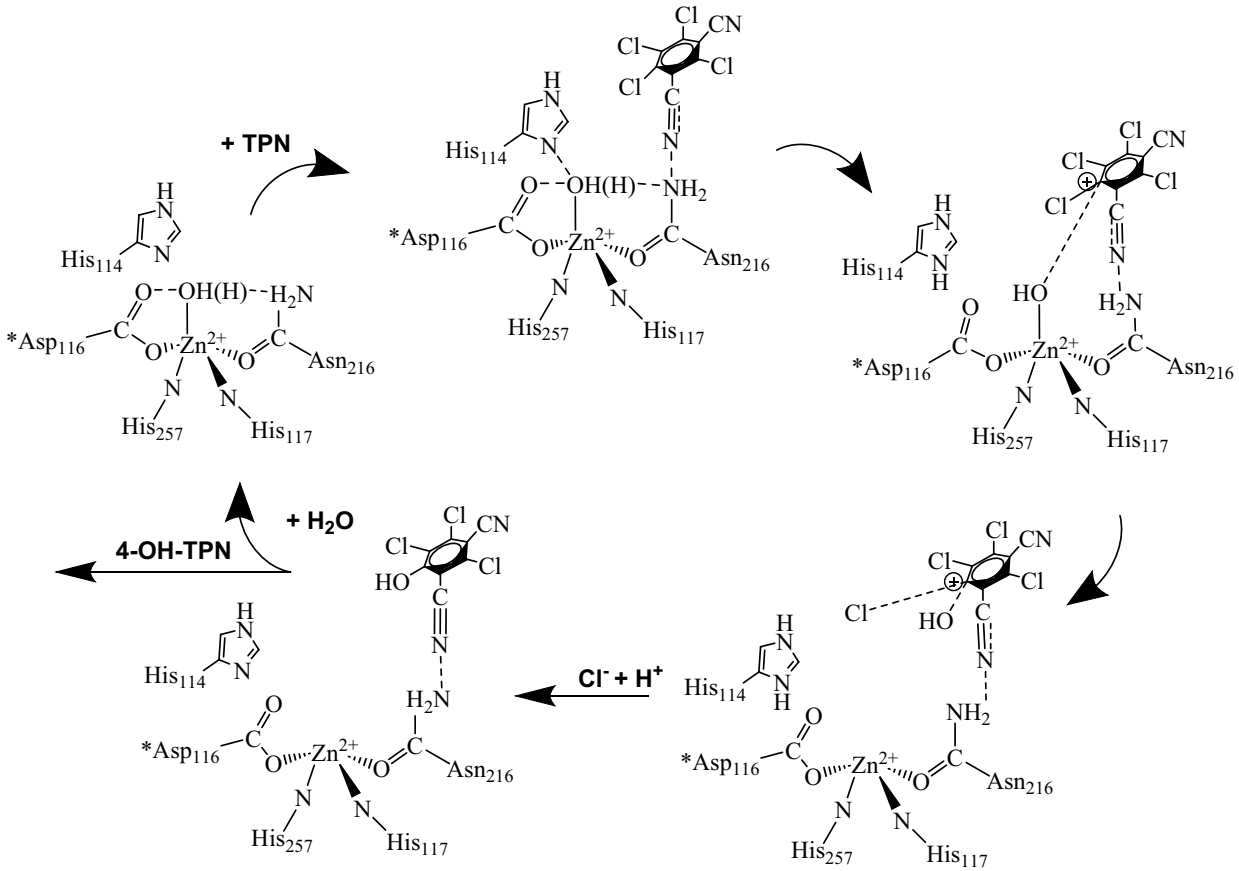

Fig. 8 Proposed mechanism for TPN hydrolysis by Chd, where His114 deprotonates the active site water (* = assisted by Asp116) as TPN coordinates to Asn216. The Zn(II) bound hydroxyl nucleophilically attacks the substrate to produce 4-OH-TPN

Asp116, the proposed role of Asn216 in forming a hydrogen bond with a CN group of TPN, and the docking study contained herein [8, 19].

Conclusion

In conclusion, the role of His114 in the context of other key residues within the active site of Chd has been refined through a hybrid set of experimental and computational techniques. Replacement of His114 by an Ala residue results in a > 95% decrease in k_{cat}, indicating His114 plays an important catalytic role but is not essential. Additionally, pH dependent kinetic assays of Chd^{H114A} reveal a pK_a of ~ 3.8, which agrees with reported pK_as of aspartic or glutamic acid residues. Thus, it is clear that His114 is not the sole active site residue that can function as the general acid/base but in its absence, deprotonation of the Zn(II)-bound water/hydroxide can likely be accomplished, albeit less efficiently, by Asp116. Based on these data and prior studies, we propose an updated mechanism for TPN hydrolysis by Chd (Fig. 8). Initially, TPN enters the active site through the substrate channel and is oriented in the substrate pocket through π–π stacking interactions with Trp227 [8, 19]. The TPN-nitrile nitrogen can form a hydrogen bond to the carboxamide nitrogen of Asn216, removing electron density from the aromatic ring and activating the ortho carbon for nucleophilic attack while simultaneously positioning TPN orthogonal to the Zn(II) center and the active site water. Deprotonation of the active site water is assisted by His114 but in its absence, another residue in the enzyme active site will need to play the role of general acid/base with the most likely candidate being Asp116. The increased rigidity of the Chd^{H114A} active site, as evidenced by EPR and MD simulations, coupled with the drastically diminished activity of the variant, suggests that the flexibility conferred by His114 is critical to catalysis. The flexibility visible in the crystal conformations of His114 is even more pronounced in a dynamic environment, where it is capable of moving nearly 2 Å, breaking the hydrogen bond between His114 and the active site water. Throughout simulation timescales, the active site conformations generated by the His114 mobility results in an improved hydrophobic substrate pocket. After catalysis, His114 mobility may allow the release of the product, 4-OH-TPN, and recharge of the active site water/hydroxide.

Supplementary Information The online version contains supplementary material available at https://doi.org/10.1007/s00775-024-02053-1.

Acknowledgements This work was supported by the National Science Foundation (CHE-2003861, RCH, CHE-1808711, RCH & BB; CHE-1532168 BB & RCH), the Todd Wehr Foundation, Bruker Biospin, and the National Institutes of Health/NIBIB National Biomedical EPR Center (P41-EB001980).

Data availability The authors declare that the key data supporting the findings of this study are available within the paper and its Supplementary Information files. Additional raw data is available on GitHub at https://github.com/Kivean/his114chd, or available on request by contacting the authors.

Declarations

Conflict of interest The authors declare that there is no conflict of interest.

References

1. Chen H, Wang H, Wang T, et al (2016) Identification of the metal center of chlorothalonil hydrolytic dehalogenase and enhancement of catalytic efficiency by directed evolution. Appl Environ Biotechnol 1:30–37. https://doi.org/10.26789/AEB.2016.01.003
2. Meng C, He Q, Huang JW et al (2015) Degradation of chlorothalonil through a hydrolytic dehalogenase secreted from Bacillus subtilis WB800. Int Biodeterior Biodegradation 104:97–104. https://doi.org/10.1016/j.ibiod.2015.05.017
3. Van Scoy AR, Tjeerdema RS (2014) Environmental fate and toxicology of Chlorothalonil. In: reviews of environmental contamination and toxicology. pp 89–105
4. De Jong RM, Dijkstra BW (2003) Structure and mechanism of bacterial dehalogenases: different ways to cleave a carbon-halogen bond. Curr Opin Struct Biol 13:722–730. https://doi.org/10.1016/j.sbi.2003.10.009
5. Qiao W, Liu G, Li M et al (2022) Complete reductive dechlorination of 4-hydroxy-chlorothalonil by dehalogenimonas populations. Environ Sci Technol 56:12237–12246. https://doi.org/10.1021/acs.est.2c02574
6. Lal D, Pandey H, Lal R (2022) Phylogenetic analyses of microbial hydrolytic dehalogenases reveal polyphyletic origin. Indian J Microbiol 62:651–657. https://doi.org/10.1007/s12088-022-01043-8
7. Huang Y, Wen L, Zhang L et al (2023) Community-integrated multi-omics facilitates screening and isolation of the organohalide dehalogenation microorganism. The Innovation 4:100355. https://doi.org/10.1016/j.xinn.2022.100355
8. Catlin DS, Yang X, Bennett B et al (2020) Structural basis for the hydrolytic dehalogenation of the fungicide chlorothalonil. J Biol Chem. https://doi.org/10.1074/jbc.ra120.013150
9. Jin X, Cui N, Zhou W et al (2014) Soil genotoxicity induced by successive applications of chlorothalonil under greenhouse conditions. Environ Toxicol Chem. https://doi.org/10.1002/etc.2538
10. Singh BK, Walker A, Wright DJ (2002) Persistence of chlorpyrifos, fenamiphos, chlorothalonil, and pendimethalin in soil and their effects on soil microbial characteristics. Bull Environ Contam Toxicol. https://doi.org/10.1007/s00128-002-0045-2
11. Kazos EA, Nanos CG, Stalikas CD, Konidari CN (2008) Simultaneous determination of chlorothalonil and its metabolite 4-hydroxychlorothalonil in greenhouse air: dissipation process of chlorothalonil. Chemosphere 72:1413–1419. https://doi.org/10.1016/j.chemosphere.2008.05.044
12. Chaves A, Shea D, Cope WG (2007) Environmental fate of chlorothalonil in a Costa Rican banana plantation. Chemosphere 69:1166–1174. https://doi.org/10.1016/j.chemosphere.2007.03.048
13. Mozzachio AM, Rusiecki JA, Hoppin JA et al (2008) Chlorothalonil exposure and cancer incidence among pesticide

applicator participants in the agricultural health study. Environ Res 108:400–403. https://doi.org/10.1016/j.envres.2008.07.018
14. Rydz E, Larsen K, Peters CE (2021) Estimating exposure to three commonly used, potentially carcinogenic pesticides (Chlorolathonil, 2,4-D, and Glyphosate) among agricultural workers in Canada. Ann Work Expo Health 65:377–389. https://doi.org/10.1093/annweh/wxaa109
15. Sandstrom MW, Nowell LH, Mahler BJ, Van Metre PC (2022) New-generation pesticides are prevalent in California's Central Coast streams. Sci Total Environ 806:150683. https://doi.org/10.1016/j.scitotenv.2021.150683
16. Kiefer K, Bader T, Minas N et al (2020) Chlorothalonil transformation products in drinking water resources: widespread and challenging to abate. Water Res 183:116066. https://doi.org/10.1016/j.watres.2020.116066
17. Yang X, Bennett B, Holz RC (2019) Insights into the catalytic mechanism of a bacterial hydrolytic dehalogenase that degrades the fungicide chlorothalonil. J Biol Chem. https://doi.org/10.1074/jbc.RA119.009094
18. Garau G, Bebrone C, Anne C et al (2005) A metallo-β-lactamase enzyme in action: crystal structures of the monozinc carbapenemase CphA and its complex with biapenem. J Mol Biol 345:785–795. https://doi.org/10.1016/j.jmb.2004.10.070
19. Yang X, Diviesti K, Miller C et al (2023) Insights into the catalytic mechanism of the chlorothalonil dehalogenase from Pseudomonas sp. CTN-3. Front Chem Biol. https://doi.org/10.3389/fchbi.2023.1105607
20. Kwon JW, Armbrust KL (2006) Degradation of chlorothalonil in irradiated water/sediment systems. J Agric Food Chem 54:3651–3657. https://doi.org/10.1021/jf052847q
21. Bennett B (2010) EPR of Cobalt-Substituted Zinc Enzymes
22. Stoll S, Schweiger A (2006) EasySpin, a comprehensive software package for spectral simulation and analysis in EPR. J Magn Reson 178:42–55. https://doi.org/10.1016/j.jmr.2005.08.013
23. (2022) Matlab version: 9.13.0 (R2022b)
24. Abraham MJ, Murtola T, Schulz R et al (2015) Gromacs: High performance molecular simulations through multi-level parallelism from laptops to supercomputers. SoftwareX 1–2:19–25. https://doi.org/10.1016/j.softx.2015.06.001
25. Pronk S, Páll S, Schulz R et al (2013) GROMACS 4.5: A high-throughput and highly parallel open-source molecular simulation toolkit. Bioinformatics 29:845–854. https://doi.org/10.1093/bioinformatics/btt055
26. Brooks BR, Brooks CL, Mackerell AD et al (2009) CHARMM: the biomolecular simulation program. J Comput Chem 30:1545–1614. https://doi.org/10.1002/jcc.21287
27. Lemkul JA (2019) From proteins to perturbed hamiltonians: a suite of tutorials for the GROMACS-2018 molecular simulation package [Article v1.0]. 1:1–53
28. Oelschlaeger P, Schmid RD, Pleiss J (2003) Insight into the mechanism of the IMP-1 metallo-β-lactamase by molecular dynamics simulations. Protein Eng 16:341–350. https://doi.org/10.1093/protein/gzg049
29. Sousa SF, Fernandes PA, Ramos MJ (2010) Molecular dynamics simulations: difficulties, solutions and strategies for treating metalloenzymes. pp 299–330
30. Croitoru A, Park S-J, Kumar A et al (2021) Additive CHARMM36 force field for nonstandard amino acids. J Chem Theory Comput 17:3554–3570. https://doi.org/10.1021/acs.jctc.1c00254
31. Maciejewski MW, Schuyler AD, Gryk MR et al (2017) NMRbox: a resource for biomolecular NMR computation. Biophys J. https://doi.org/10.1016/j.bpj.2017.03.011
32. Korb O, Stützle T, Exner TE (2009) Empirical scoring functions for advanced protein−ligand docking with plants. J Chem Inf Model 49:84–96. https://doi.org/10.1021/ci800298z
33. Dreyton CJ, Knuckley B, Jones JE et al (2014) Mechanistic studies of protein arginine deiminase 2: evidence for a substrate-assisted mechanism. Biochemistry 53:4426–4433. https://doi.org/10.1021/bi500554b
34. Sivo V, D'Abrosca G, Russo L et al (2017) Co(II) coordination in prokaryotic zinc finger domains as revealed by UV-Vis spectroscopy. Bioinorg Chem Appl 2017:1–7. https://doi.org/10.1155/2017/1527247
35. Cass ME, Hii KK, Rzepa HS (2006) Mechanisms that interchange axial and equatorial atoms in fluxional processes: illustration of the berry pseudorotation, the turnstile, and the lever mechanisms via animation of transition state normal vibrational modes. J Chem Educ 83:336. https://doi.org/10.1021/ed083p336.2
36. Harris TK, Mildvan AS (1999) High-precision measurement of hydrogen bond lengths in proteins by nuclear magnetic resonance methods. Prot Str Funct Genet 35:275–282. https://doi.org/10.1002/(SICI)1097-0134(19990515)35:3
37. Steinert RM, Kasireddy C, Heikes ME, Mitchell-Koch KR (2022) Newly identified C-H···O hydrogen bond in histidine. Phys Chem Chem Phys 24:19233–19251. https://doi.org/10.1039/d2cp02048c
38. Sakurai M, Furuki T, Inoue Y (1995) The pKa of the zinc-bound water in carbonic anhydrase and its model compounds as studied by the AM1 calculation coupled with a reaction field theory. J Phys Chem 99:17789–17794. https://doi.org/10.1021/j100050a019
39. Silverstein TP, Heller ST (2017) Values in the undergraduate curriculum: what is the real pKa of water? J Chem Educ 94:690–695. https://doi.org/10.1021/acs.jchemed.6b00623
40. González JM (2021) Visualizing the superfamily of metallo-β-lactamases through sequence similarity network neighborhood connectivity analysis. Heliyon. https://doi.org/10.1016/j.heliyon.2020.e05867
41. Simona F, Magistrato A, Dal M et al (2009) Common mechanistic features among Metallo-β-lactamases. J Biol Chem 284:28164–28171. https://doi.org/10.1074/jbc.M109.049502
42. Meini M, Llarrull LI, Vila AJ (2015) Overcoming differences: The catalytic mechanism of metallo- b -lactamases. FEBS Lett 589:3419–3432. https://doi.org/10.1016/j.febslet.2015.08.015
43. Bottari E, Festa MR (1996) Asparagine as a ligand for cadmium(II), lead(II) and zinc(II). Chem Speciat Bioavailab 8:75–83. https://doi.org/10.1080/09542299.1996.11083272
44. Sciences ML, Vanhove M, Zakhem M et al (2003) Role of Cys221 and Asn116 in the zinc-binding sites of the Aeromonas hydrophila metallo- b -lactamase. Cell Mol Life Sci CMLS 60:2501–2509. https://doi.org/10.1007/s00018-003-3092-x
45. Çlnaroğlu SS, Timuçin E (2019) Comparative Assessment of Seven Docking Programs on a Nonredundant Metalloprotein Subset of the PDBbind Refined. J Chem Inf Model. https://doi.org/10.1021/acs.jcim.9b00346
46. (2008) Guide to the Expression of Uncertainty in Measurement (GUM). 98